Dalton Transactions

ROYAL SOCIETY OF CHEMISTRY

PAPER

View Article Online
View Journal | View Issue

Cite this: *Dalton Trans.*, 2026, **55**, 173

Solvent- and metal-gated coordination diversity in a dynamic aminal ligand

Jen-Wen Juan,[a] Ji-Ming Ciou,[b] Yi-Rong Hsiang†[a,c] and Ya-Fan Lin *[a]

Received 7th October 2025,
Accepted 1st December 2025

DOI: 10.1039/d5dt02405f

rsc.li/dalton

Within the broad landscape of dynamic covalent chemistry (DCC), the coordination chemistry of primary-amine-based aminals has received comparatively little systematic investigation. Here we demonstrate that a primary-amine-based dynamic covalent aminal (L^{A2}) can serve as an adaptive scaffold for coordination chemistry diversity, where solvent and metal ion choice govern distinct outcomes. Coordination stabilizes otherwise transient ligand forms and directs divergent pathways: Co(III) stabilizes hemiaminalates in methanol, with $[Co(L^{O2})_2](ClO_4)$ exhibiting fluxional behavior, and templates macrocyclization in acetonitrile to yield $[Co(L^{M})](ClO_4)_3$; Cu(II) affords hemiaminal and hemiaminal ether complexes, and Fe(III) promotes pyridinium dimerization to give *cis*-$[(L^{I2})_2](ClO_4)$. These findings establish that dynamic ligands can actively generate structural diversity in metal complexes, opening new directions for adaptive ligand design and functional coordination architectures.

Introduction

Primary-amine-based aminals can be considered as precursors to imines,[1–4] and many systems exist in reversible equilibrium between imine and aminal forms, displaying dynamic covalent properties.[5–8] Imines are versatile scaffolds in organic synthesis, sensing, and materials chemistry,[9–17] and their reversibility has been widely exploited in dynamic covalent chemistry (DCC) to construct adaptive and responsive molecular architectures.[18–25] While DCC has often been applied to macromolecular self-assemblies and higher-order structures,[26–33] its potential in stabilizing transient small-molecule species through metal coordination remains comparatively underexplored.[34–38]

Dynamic aminals derived from primary amines readily interconvert with imines, which in turn serve as competent ligands for metal coordination. Although imines possess lower electrophilicity than both iminium ions and aldehydes/ketones, they can still undergo nucleophilic addition, thereby providing access to otherwise elusive species such as hemiaminals and hemiaminal ethers. Notably, most metal-stabilized hemiaminal or hemiaminal-ether systems reported to date arise from secondary amines or cyclic aminals.[39–45] In contrast, primary-amine-based aminals enable a broader set of interconnected equilibria involving imines, hemiaminals, and hemiaminal ethers, yet their coordination behaviour has been far less systematically explored. In this context, Anslyn and co-workers established a highly adaptive Zn(II)-templated dynamic system that provides a key precedent. In their framework, 2-pyridinecarboxaldehyde (2-PA) and 4-methylaniline first generate an imine, and subsequent addition of the secondary amine di(2-picolyl)amine (DPA) leads to dynamic metal-templated assemblies.[38] They further demonstrated aniline-exchange behaviour using *para*-substituted anilines, with more electron-donating anilines displaying larger equilibrium constants. In a related Zn(II)/2-PA/DPA system, they also showed reversible formation of hemiaminals and hemiaminal ethers upon alcohol addition,[37,46] as well as aminal-type complexes upon introducing secondary amines.[47]

In our prior work (Scheme 1), we developed primary-amine-based heterocyclic aminals L^{A1} and L^{A2}, both of which display solvent- and condition-dependent equilibria, generating imines, hemiaminals, and hemiaminal ethers that are detectable in solution but difficult to isolate.[7] Previous studies of L^{A1}-related complexes largely emphasized structural characterization, without probing their underlying equilibria or adaptive properties.[48–51] In contrast, the present study systematically investigated L^{A2} as a dynamic covalent ligand in coordination chemistry. Inspired by the adaptivity observed in Anslyn's system, we explored whether coordination to different metal ions in different solvent systems could stabilize these inherently dynamic forms, enabling structural characterization and directing their reactivity along divergent pathways. A criti-

[a]*Department of Chemistry, National Dong Hwa University, Hualien 974301, Taiwan. E-mail: yafan@gms.ndhu.edu.tw*
[b]*PhD Program in Life Science, College of Life Science, Kaohsiung Medical University, Kaohsiung 807378, Taiwan*
[c]*Department of Medicinal and Applied Chemistry, Kaohsiung Medical University, Kaohsiung 807378, Taiwan*
†Current affiliation: Department of Chemistry, National Taiwan Normal University, Taipei 11677, Taiwan.

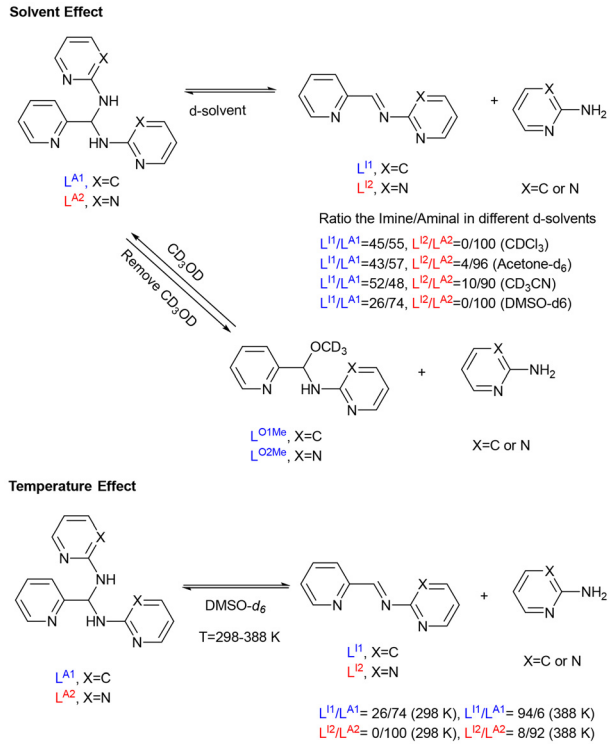

Scheme 1 A summary for the dynamic covalent properties for aminals L^{A1} and L^{A2}.

cal question is whether such dynamic ligands can be deliberately harnessed to expand structural diversity in metal complexes.

This study demonstrates that dynamic covalent ligand L^{A2} can act as an adaptive scaffold for coordination chemistry diversity. Coordination stabilizes otherwise transient ligand forms and directs their reactivity along divergent pathways: Co(III) stabilizes hemiaminalates in methanol and templates macrocyclization in acetonitrile, Cu(II) stabilizes hemiaminals or hemiaminal ethers, and Fe(III) induces pyridinium dimerization.[52] These findings establish a conceptual framework in which dynamic covalent ligands serve not merely as passive participants but as active drivers of coordination diversity, opening new directions for adaptive ligand design and functional coordination architectures.

Results and discussion

Influence of solvent

Given the ability of the dynamic aminal systems of L^{A1} and L^{A2} to reversibly transform into hemiaminal ether and imine through solvent tuning, we initiated an investigation into the coordination chemistry of these dynamic ligands by examining their behaviour in various solvents in the presence of metal ions.

Methanol as the solvent. Although the hemiaminal ether L^{O2Me} can be detected only in the methanol solution, the addition of $Co(ClO_4)_2{\cdot}6H_2O$ enables one-pot reaction of two equivalents of 2-PA with 2-aminopyrimidine in methanol under aerobic conditions, affording a Co(II) complex of the hemiaminal ether, $[Co(L^{O2Me})_2](ClO_4)_2$ (Scheme 2). The UV-Vis absorption spectrum of $[Co(L^{O2Me})_2](ClO_4)_2$ exhibits a d–d transition band at λ_{max} = 487 nm (ε = 97 M^{-1} cm^{-1}). X-ray diffraction crystallography (Fig. 1(a)) confirmed a centrosymmetric structure in which two hemiaminal ether ligands coordinate to Co(II) in a facial arrangement.

$[Co(L^{O2Me})_2](ClO_4)_2$ is unstable in air, undergoing gradual oxidation to give a pink powder. After purification and characterization, the product was identified as the Co(III) complex, $[Co(L^{O2})_2](ClO_4)$, which crystallizes in an non-centrosymmetric structure within the monoclinic space group $P2_1/c$ (Fig. 1(b)). The two Co–O bond lengths (1.894(2), 1.892(2) Å) are significantly shorter than those in $[Co(L^{O2Me})_2](ClO_4)_2$ (2.1362 (15) Å), and the four Co–N bond lengths (average ~1.95 Å) are also shorter than in $[Co(L^{O2Me})_2](ClO_4)_2$ (average ~2.13 Å). These shortened donor-Co distances enforce larger bite angles in $[Co(L^{O2})_2](ClO_4)$, reflecting the more compact geometry of a Co(III) complex.

The analogue $[Co(L^{O1})_2](ClO_4)$ has previously been reported, though only its molecular structure was described. Attempts to prepare the corresponding hemiaminal ether complex $[Co(L^{O1Me})_2](ClO_4)_2$ under aerobic conditions yielded only $[Co(L^{O1})_2](ClO_4)$. UV-Vis absorption spectra revealed that $[Co(L^{O1})_2](ClO_4)$ and $[Co(L^{O2})_2](ClO_4)$ both display d–d transition

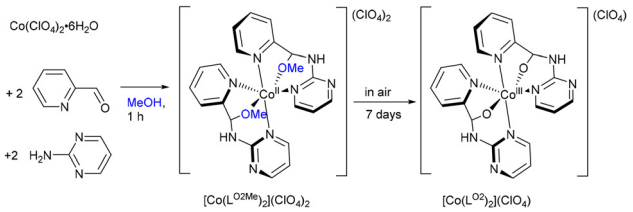

Scheme 2 One-pot synthesis for $[Co(L^{O2Me})_2](ClO_4)_2$.

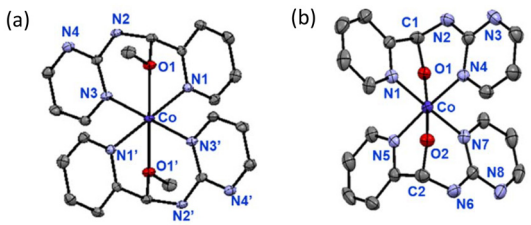

Fig. 1 ORTEP drawings of (a) $[Co(L^{O2Me})_2](ClO_4)_2$ and (b) $[Co(L^{O2})_2](ClO_4)$. The counteranion (ClO_4^-) and hydrogen atoms are omitted for clarity. Thermal ellipsoids are displayed at 50% probability level. Selected bond lengths (Å) and bond angles (°) for (a) $[Co(L^{O2Me})_2](ClO_4)_2$: Co–O1: 2.1362(15), Co–N1: 2.1202(18), Co–N3: 2.1482(18), O1–Co–N1: 75.76(6), O1–Co–N3: 85.21(6), N1–Co–N3: 87.62(7); and (b) $[Co(L^{O2})_2](ClO_4)$: Co–O1: 1.894(2), Co–O2: 1.892(2), Co–N1: 1.908(3), Co–N3: 1.971(3), Co–N5: 1.923(3), Co–N7: 1.953(3), O1–Co–O2: 175.71(9), O1–Co–N1: 84.6(1), O1–Co–N3: 90.2(1), O2–Co–N5: 84.6(1), O2–Co–N7: 89.5(1), N1–Co–N3: 89.0(1), N5–Co–N7: 90.6(1).

bands at λ_{max} = 510 nm (ε = 64 and 69 M^{-1} cm^{-1}, respectively) in methanol, indicating similar coordination geometries and comparable ligand field environments.

To improve the yield, the synthesis was optimized using a one-pot reaction of $Co(ClO_4)_2{\cdot}6H_2O$, 2-pyridinecarboxaldehyde, 2-aminopyrimidine in a 1 : 2 : 2 ratio in methanol, followed by addition of two equivalents of TBHP as oxidant and overnight stirring. Evaporation of the solvent and the recrystallization from acetone afforded $[Co(L^{O2})_2](ClO_4)$ in good yield. Interestingly, the same product can also be obtained by reacting $Co(ClO_4)_2{\cdot}6H_2O$ with two equivalents of the aminal ligand L^{A2} in methanol under aerobic conditions, without isolating the Co(II) intermediate $[Co(L^{O2Me})_2](ClO_4)_2$ (Scheme 3).

The ^{1}H NMR spectra in DMSO-d_6 showed the methine proton resonance of the hemiaminalate moieties at 5.54 ppm for $[Co(L^{O1})_2](ClO_4)$ and 5.65 ppm for $[Co(L^{O2})_2](ClO_4)$, with corresponding ^{13}C signals at 84.2 ppm and 84.6 ppm. Both complexes displayed minor isomeric species, with major /minor ratios of approximately 5 : 1 for $[Co(L^{O1})_2](ClO_4)$ and 12 : 1 for $[Co(L^{O2})_2](ClO_4)$ (Fig. S10 and S14). For $[Co(L^{O1})_2](ClO_4)$, the ratio was solvent-independent (Fig. S11 and S12), whereas for $[Co(L^{O2})_2](ClO_4)$ it varied (8 : 1 in CD_3OD and 6 : 1 in CD_3CN), underscoring the structural inertness for $[Co(L^{O1})_2](ClO_4)$ *versus* the fluxionality of $[Co(L^{O2})_2](ClO_4)$ (Fig. S15 and S16). Dissolving crystalline $[Co(L^{O2})_2](ClO_4)$ in DMSO-d_6 reproduced the same spectral features, confirming the intrinsic lability of its hemiaminalate ligands.

Density functional theory (DFT) calculations at the B3LYP-D3 level with the LanL2DZ basis set for Co and 6-31g* for H, C, and N were carried out using Gaussian 16 program.[53–55] Only isomers with equivalent hemiaminalate environments were considered, consistent with the ^{1}H NMR spectra, which showed a single set of ligand signals. As shown in Fig. 2, the crystal form OC-6-13-$[Co(L^{O2})_2]^+$ was the most stable and used as the reference. The Ci-symmetric OC-6-12-$[Co(L^{O2})_2]^+$ was only 2.0 kcal mol^{-1} higher in energy, whereas OC-6-22- and OC-6-33-$[Co(L^{O2})_2]^+$ were 11.0 and 12.7 kcal

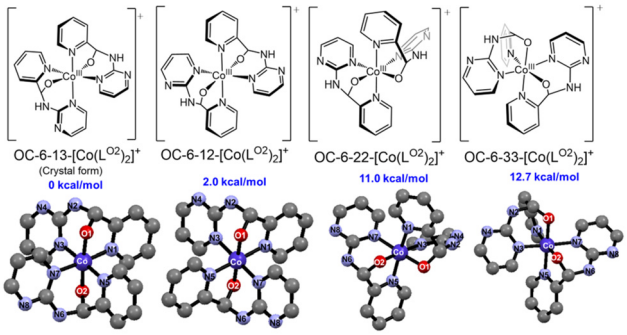

Fig. 2 Schematic representations and optimized structures of the possible isomers, along with their relative potential energies. The isomer names follow the configuration index system recommended by IUPAC.[56]

mol^{-1} less stable, suggesting they are minor species. Accordingly, the major and minor isomers observed in solution were assigned to OC-6-13-$[Co(L^{O2})_2]^+$ and OC-6-12-$[Co(L^{O2})_2]^+$, respectively. The increased OC-6-13-$[Co(L^{O2})_2]^+$/OC-6-12-$[Co(L^{O2})_2]^+$ ratio in polar solvents correlates with their calculated dipole moments (41.5 D *vs.* 0 D), indicating the solvent polarity governs the isomer distribution.

Interestingly, $[Co(L^{O2})_2](NO_3)$ can be obtained by replacing $Co(ClO_4)_2{\cdot}6H_2O$ with $Co(NO_3)_2{\cdot}6H_2O$. Its NMR spectra resembled those of $[Co(L^{O2})_2](ClO_4)$, showing two sets of ^{1}H NMR signals but with smaller major/minor ratios of 1.6 : 1, 2.5 : 1 and 3.5 : 1 in DMSO-d_6, CD_3OD, and CD_3CN, respectively (Fig. S18–S20). This facilitated the isolation of two distinct crystals from CH_3CN: one non-centrosymmetric, analogous to $[Co(L^{O2})_2](ClO_4)$, and one centrosymmetric, corresponding to the predicted iso1-$[Co(L^{O2})_2]^+$ (Fig. S1(a) and (b)). Occasionally, we also obtained neutral $[Co(L^{O2})_2]$ in a centrosymmetric configuration (Fig. S1(c)), although this form was unstable and decomposed to an unidentified diamagnetic Co(III) species.

We proposed the mechanism for the conversion of $[Co(L^{O2})_2]^+$ from $[Co(L^{O2Me})_2]^{2+}$ (Scheme 4). In methanol, hemiam-

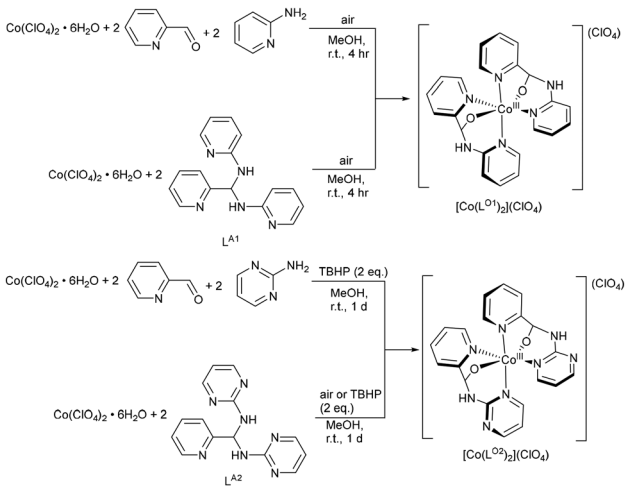

Scheme 3 Synthesis routes for $[Co(L^{O1})_2](ClO_4)$ and $[Co(L^{O2})_2](ClO_4)$.

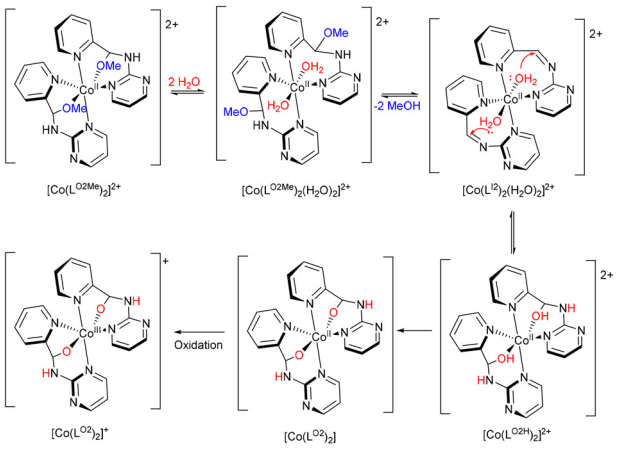

Scheme 4 Proposed mechanism for the conversion of $[Co(L^{O2})_2]^+$ from $[Co(L^{O2Me})_2]^{2+}$.

inal ether L^{O2Me} may remain metastable upon Co(II) coordination, but the –OMe moiety is labile and competes with aqua ligands from the metal ion hydration sphere or solvent. Equilibrium with $[Co(L^{O2Me})_2(H_2O)_2]^{2+}$ in solution enables elimination of methanol, giving $[Co(L^{I2})_2(H_2O)_2]^{2+}$, which undergoes intramolecular nucleophilic addition to form the hemiaminal intermediate $[Co(L^{O2H})_2]^{2+}$. Subsequent deprotonation by environmental species (*e.g.* MeOH or H_2O) furnishes $[Co(L^{O2})_2]$, which is then oxidized by air to $[Co(L^{O2})_2]^+$. When the reaction was carried out by directly reacting the pre-synthesized ligand L^{A2} with $Co(ClO_4)_2{\cdot}6H_2O$ in methanol, 2-aminopyrimidine was released during L^{O2Me} formation *in situ*. Acting as a weak base, the liberated 2-aminopyrimidine facilitates rapid deprotonation of $[Co(L^{O2H})_2]^{2+}$, accelerating its conversion to $[Co(L^{O2})_2]$ followed by oxidation. This explains why $[Co(L^{O2Me})_2](ClO_4)_2$ could not be isolated under these conditions.

Acetonitrile as the solvent. In an attempt to isolate $[Co(L^{O2H})_2](ClO_4)_2$, we dissolved $[Co(L^{O2Me})_2](ClO_4)_2$ in CH_3CN that was not rigorously dried. Unexpectedly, recrystallization from methanol afford $[Co(L^{M})](ClO_4)_3$ as a bright orange powder. Single-crystal X-ray diffraction analysis (Fig. 3) revealed that the product contains a polyazamacrocyclic ligand (Scheme 5), in which the Co(III) centre is coordinated by three pyridyl (N_{py}) and three azamacrocyclic (N_{aza}) nitrogen donors. The Co–N bond lengths are approximately 1.92 Å (N_{py}) and 1.88 Å (N_{aza}). Suitable crystals were obtained by Et_2O diffusion into CH_3CN.

$[Co(L^{M})](ClO_4)_3$ was also obtained by reacting $Co(ClO_4)_2{\cdot}6H_2O$ with three equivalents of L^{A2} in CH_3CN, or *via* one-pot reaction of $Co(ClO_4)_2{\cdot}6H_2O$, 2-PA and 2-aminopyrimidine (1 : 3 : 3) under aerobic conditions. Addition of one equivalent of $NaClO_4$ to balance the charge of Co(III) and refluxing improved the yield to 60% (Scheme 6). The ^1H NMR spectrum in DMSO-d_6 showed a methine resonance at 7.97 ppm with a corresponding ^{13}C signal at 80.3 ppm. The UV-Vis absorption spectrum in CH_3CN showed a d–d transition band at λ_{max} = 480 nm (ε = 315 M^{-1} cm^{-1}). Unlike $[Co(L^{O2})_2](ClO_4)$, $[Co(L^{M})](ClO_4)_3$ does not exhibit fluxional behaviour and is insoluble in methanol, but remains soluble and stable in CH_3CN, D_2O and DMSO-d_6. Variable–temperature NMR (VT-NMR) analysis conducted in DMSO-d_6 confirmed stability up to 403 K, above which decomposition yielded signals corresponding to 2-pyridinecarboxaldehyde and 2-aminopyrimidine (Fig. S21).

As illustrated in Scheme 7, the macrocyclic ligand L^{M} likely form through trimerization of the imino fragment. In our previous study, approximately 10% of L^{A2} is converted to L^{I2} in CD_3CN.[7] Accordingly, L^{O2Me} may undergo equilibration with L^{I2}/L^{A2}, releasing a methanol molecule in CH_3CN. Based on these observations, $[Co(L^{M})](ClO_4)_3$ formation begins with $[Co(L^{O2Me})_2]$ undergoing –OMe substitution by CH_3CN, followed by methanol elimination to form $[Co(L^{I2})_2(MeCN)_2]^{2+}$. Ligand exchange then furnishes $[Co(L^{I2})_3]^{2+}$, which undergoes intramolecular nucleophilic attack of the pyrimidyl nitrogen on the C=N group, driving cyclization to yield $[Co(L^{M})]^{3+}$. Alternatively, $[Co(L^{I2})_3]^{2+}$ can also be generated directly through Co(II) templating of three L^{I2} units, which then undergo nucleophilic addition to produce $[Co(L^{M})]^{3+}$ (Scheme 7). Consistently, when acetone was used as solvent, $[Co(L^{M})](ClO_4)_3$ was also obtained, albeit in slightly lower yield (45%), possibly due to reduced L^{I2} formation under these conditions.

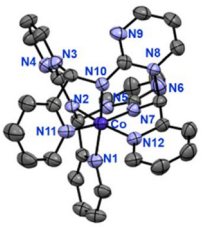

Fig. 3 ORTEP drawing of $[Co(L^{M})](ClO_4)_3$. The counteranion (ClO_4^-) and hydrogen atoms are omitted for clarity. Thermal ellipsoids are displayed at 50% probability level. Selected bond lengths (Å) and bond angles (°) for $[Co(L^{M})](ClO_4)_3$: Co–N1: 1.928 (7); Co–N2: 1.872(7); Co–N7: 1.880(7); Co–N10: 1.881(7); Co–N11: 1.925(8); Co–N12: 1.920(7); N(1)–Co(1)–N(2): 83.7(3); N(7)–Co(1)–N(12): 83.7(3); N(10)–Co(1)–N(11): 83.6(3); N(1)–Co(1)–N(7): 91.5(3); N(1)–Co(1)–N(12): 97.0(3); N(1)–Co(1)–N(11): 95.8(3); N(2)–Co(1)–N(7): 88.8(3); N(2)–Co(1)–N(10): 88.8(3); N(2)–Co(1)–N(11): 89.4(3); N(7)–Co(1)–N(10): 88.9(3); N(10)–Co(1)–N(12): 90.5(3); N(11)–Co(1)–N(12): 97.9(3).

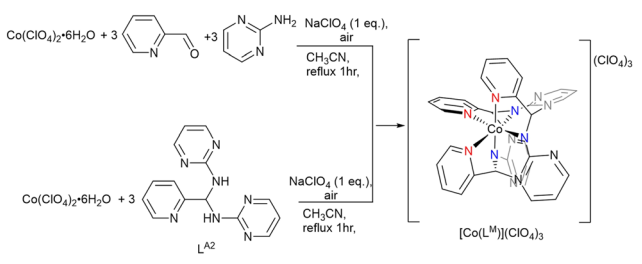

Scheme 5 Polyazamacrocyclic structure of $[Co(L^{M})](ClO_4)_3$ with pyridyl donors (N_{py}) highlighted in red, and azamacrocyclic donors (N_{aza}) in blue. The macrocyclic ligand is generated through trimerization of three L^{I2} units.

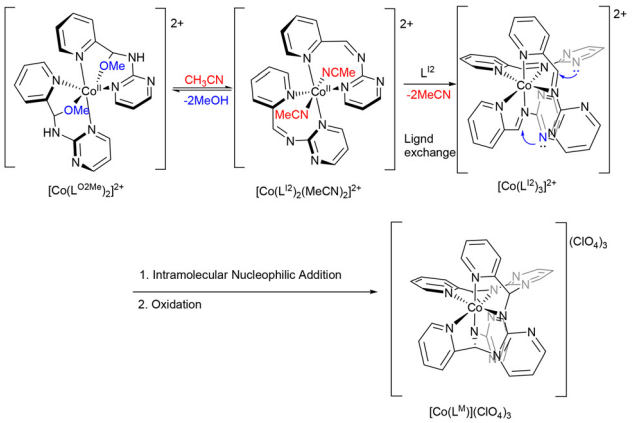

Scheme 6 Synthetic routes for $[Co(L^{M})](ClO_4)_3$.

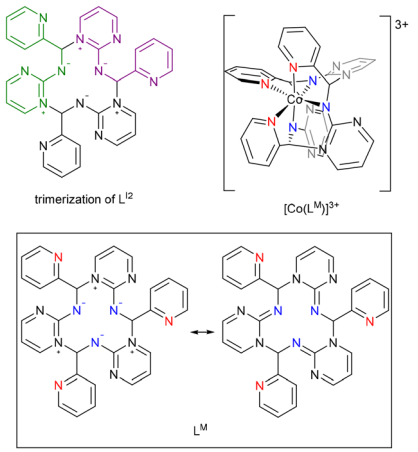

Scheme 7 Proposed mechanism for the formation of $[Co(L^M)](ClO_4)_3$.

To obtain the free macrocyclic ligand L^M, demetalation of $[Co(L^M)](ClO_4)_3$ was attempted by adding either HCl or NaCN (six equivalents) in MeCN under reflux conditions.[57] However, HCl left the complex unchanged, while NaCN led to decomposition reactions. Considering that Co(II) is more labile than Co(III), potentially facilitating demetalation, a reductant, such as $NaBH_4$ or Zn dust was introduced to the reaction mixture to enhance the likelihood of successful demetalation.[58,59] Unfortunately, this approach only yielded the amine, L^{A2}-re, the reduction product of L^{A2} (Scheme 8). Analysis of the redox properties of $[Co(L^M)](ClO_4)_3$ provides insight into this outcome. Cyclic voltammetry of a 10 mM solution of $[Co(L^M)](ClO_4)_3$ in DMSO, using 0.1 M $[NBu_4][ClO_4]$ as a supporting electrolyte and a 50 mV s^{-1} scan rate, was performed in the potential range of 1.0 to −2.0 V. During the anodic scan, no corresponding anodic peak was observed, whereas the cathodic scan exhibits peaks at −0.370, −0.646, and −1.224 V *vs.* Fc/Fc^+ (Fig. S22), corresponding to the reduction of the ligand, the Co(III)/Co(II) transition and Co(II)/Co(I) transition, respectively.[60–63] The experimental results suggest that the macrocyclic ligand L^M undergoes reduction when treated with Zn dust, a mild reductant, with a reduction potential of −0.76 V.[64] The observed formation of $[Co(L^M)](ClO_4)_3$ is likely driven by its thermodynamic stability through self-assembly. Attempts to isolate the free ligand L^M using acid, base or alternative demetalation strategies were unsuccessful.

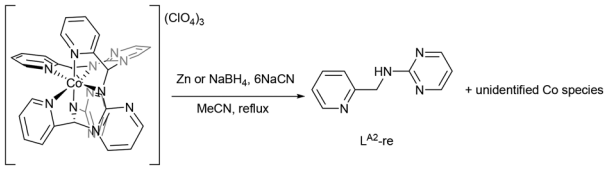

Scheme 8 Demetalation reactions of $[Co(L^M)](ClO_4)_3$ only yield an amine L^{A2}-re.

Influence of metal ion

We next explored the coordination behaviour of $Cu(ClO_4)_2{\cdot}6H_2O$ toward the picolyl heterocyclic amino aminals L^{A1} and L^{A2}. In methanol, the reactions under aerobic conditions afforded $[Cu(L^{O1Me})_2](ClO_4)_2$ and $[Cu(L^{O2Me})_2](ClO_4)_2$ as green and blue powders, respectively (Scheme 9). Slow evaporation of methanol yielded single crystals suitable for X-ray diffraction. As shown in Fig. 4(a) and (b), both complexes crystallize in centrosymmetric structures with the space groups $P2_1/c$. The Cu–O bond lengths (~2.4 Å) fall within the range

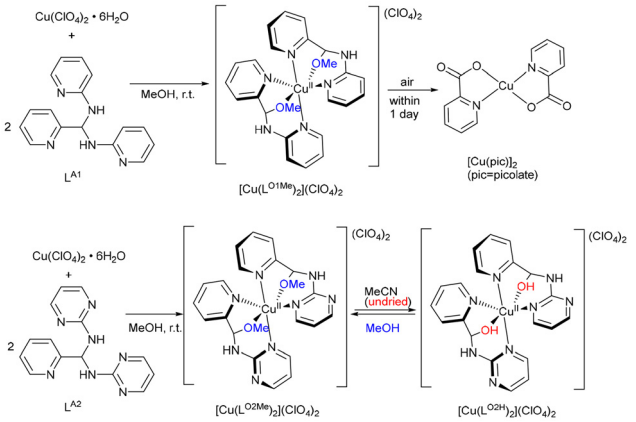

Scheme 9 Reactions of L^{A1} and L^{A2} with $Cu(ClO_4)_2{\cdot}6H_2O$ to generate $[Cu(L^{O1Me})_2](ClO_4)_2$, $[Cu(L^{O2Me})_2](ClO_4)_2$ and $[Cu(L^{O2H})_2](ClO_4)_2$.

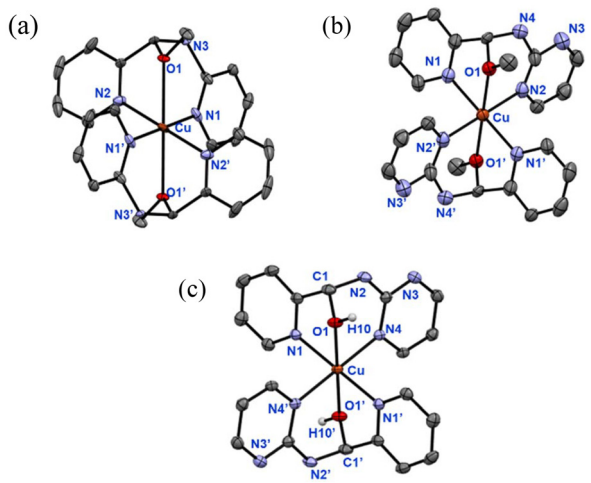

Fig. 4 ORTEP drawing of (a) $[Cu(L^{O1Me})_2](ClO_4)_2$, (b) $[Cu(L^{O2Me})_2](ClO_4)_2$, and (c) $[Cu(L^{O2H})_2](ClO_4)_2$. Counteranions are omitted for clarity; hydrogen atoms, except for the ones on the hemiaminal moiety, are also omitted. Thermal ellipsoids are displayed at 50% probability level. Selected bond lengths (Å) and bond angles (°) for (a) $[Cu(L^{O1Me})_2](ClO_4)_2$: Cu–O1: 2.433 (6); Cu–N1: 2.015(4); Cu–N2: 2.022(4); N1–Cu–O1: 89.8 (2); N2–Cu–O1: 71.7(2); N1–Cu–N2: 89.47(19). (b) $[Cu(L^{O2Me})_2](ClO_4)_2$: Cu–O1: 2.398(5); Cu–N1: 2.013(3); Co–N2: 2.042(3); N1–Cu–O1: 72.23 (14); N2–Cu–O1: 87.05(14); N1–Cu–N2: 89.17(11). (c) $[Cu(L^{O2H})_2](ClO_4)_2$: Cu–N1: 1.993(2); Cu–N3: 2.0816(19); Cu–O1: 2.2819(17); O1–H10: 0.89 (4); N1–Cu–O1: 76.82(7); N1–Cu–N3: 89.34(8); O1–Cu–N3: 84.50(7).

typically observed for Cu(II)-neutral alcohol interaction,[65–67] suggesting relatively weak coordination. The $[Cu(L^{O1Me})_2](ClO_4)_2$ crystals were unstable in air, transforming into purple $[Cu(pic)_2]$ (pic = picolinate).

In contrast, recrystallization of $[Cu(L^{O2Me})_2](ClO_4)_2$ from CH_2Cl_2/CH_3CN yielded $[Cu(L^{O2H})_2](ClO_4)_2$, instead of a macrocyclic Cu(II) complex. Blue block-shape crystals of $[Cu(L^{O2H})_2](ClO_4)_2$ were obtained by diffusing CH_2Cl_2 into an CH_3CN solution. X-ray diffraction analysis (Fig. 4(c)) revealed a Cu(II) centre coordinated by two hemiaminal ligands, with Cu–O bond lengths of 2.2819(17), shorter than those observed in $[Cu(L^{O2Me})_2](ClO_4)_2$. Thus, $[Cu(L^{O2H})_2](ClO_4)_2$ can be prepared directly from $Cu(ClO_4)_2{\cdot}6H_2O$ and two equivalents of L^{A2} in CH_3CN.

Interestingly, redissolving $[Cu(L^{O2H})_2](ClO_4)_2$ in methanol and recrystallized by slow solvent evaporation regenerated $[Cu(L^{O2Me})_2](ClO_4)_2$. Likewise, HR-ESI-MS analysis revealed that dissolving $[Cu(L^{O2H})_2](ClO_4)_2$ in ethanol led to the formation of $[Cu(L^{O2Et})_2](ClO_4)_2$ (Fig. S31). These observations demonstrate that solvent choice (alcohol *vs.* non-alcohol) directs whether the Cu(II) centre coordinates to the hemiaminal ether or the hemiaminal ligands (Scheme 9). Consistent with its dynamic behaviour in solution, $[Cu(L^{O2H})_2](ClO_4)_2$ exhibits distinct d–d transition bands: λ_{max} = 656 nm (ε = 144 M^{-1} cm^{-1}) in methanol and λ_{max} = 689 nm (ε = 89 M^{-1} cm^{-1}) in CH_3CN.

DFT study of the formation of macrocyclic complex

We are intrigued by the novel macrocyclic L^M structure and aim to address the following questions through calculations: (1) Under what conditions can the macrocyclic structure form? (2) Why does the Cu(II) system fail to yield the macrocyclic structure? Based on our hypothesis shown in Scheme 7, we performed simulations of $[Co(L^{I2})_3]^{3+}$ and $[Co(L^M)]^{3+}$ to explore the structural and energetic factors that govern the formation of the macrocyclic structure. The calculations were performed at the same level of theory previously applied to the isomers for $[Co(L^{O2})]^+$.

The optimized structure of $[Co(L^{I2})_3]^{3+}$ shows that the three L^{I2} ligands coordinate with Co(III) in a bidentate manner through the pyridyl N and imine N atoms. Additionally, we identified an n → π* interaction between the pyrimidyl N atom and the C=N bond of the adjacent L^{I2} ligand (depicted by green dashed line in Fig. 5),[68–72] with an energy of 0.58 kcal mol^{-1}. The Bürgi-Dunitz (BD) trajectory parameters, including BD angle (α = 86.4°, the N–C–N angle in Fig. 5),[73] were calculated, and the N–C distance (d) was found to be 2.77 Å,[74–76] which is smaller than the sum of the van der Waals radii of N and C (3.25 Å). These findings suggest a significant intramolecular n → π* interaction between the pyrimidyl N and the adjacent C=N bond. When comparing the potential energies of $[Co(L^{I2})_3]^{3+}$ and $[Co(L^M)]^{3+}$, we found that $[Co(L^M)]^{3+}$ is 24.5 kcal mol^{-1} more stable, which explains why the reaction favours the formation of the macrocyclic $[Co(L^M)](ClO_4)_3$, driven by its thermodynamic stability.

Conversely, when Cu(II) is used as the central metal, the simulated $[Cu(L^{I2})]^{2+}$ shows an intramolecular n → π* interaction with an energy of 0.25 kcal mol^{-1}. The N–C distance in this case is 3.26 Å, which is nearly equal to the sum of the van der Waals radii of N and C, indicating a much weaker n → π* interaction in $[Cu(L^{I2})_3]^{2+}$ compared to $[Co(L^{I2})_3]^{3+}$. Furthermore, the potential energy of $[Cu(L^{I2})]^{2+}$ is 7.24 kcal mol^{-1} lower than $[Cu(L^M)]^{3+}$, suggesting that the formation of the macrocyclic L^M complex is thermodynamically unfavourable in the Cu(II) system. The electron-deficient nature of the C=N bond after Cu(II) coordination makes it susceptible to attack by water molecules, leading to the formation of $[Cu(L^{O2H})_2]^{2+}$.

To further explore the formation of the metal complexes with the macrocyclic L^M ligand beyond $[Co(L^M)]^{3+}$, we performed theoretical calculations on 12 metal ions (Sc^{3+}, Ti^{2+}, Ti^{4+}, V^{2+}, Cr^{2+}, Mn^{2+}, Fe^{2+}, Fe^{3+}, Co^{2+}, Ni^{2+}, Zn^{2+}, and Al^{3+}). We compared the potential energies of $[M(L^{I2})_3]^{n+}$ and $[M(L^M)]^{n+}$ structures (Fig. 6) and examined the presence of interactions between the pyrimidyl N and the C=N bond of the adjacent L^{I2} ligand in $[M(L^{I2})_3]^{n+}$. The results are summarized in Table 1. From the calculations, Ti^{2+} and Mn^{2+} exhibit relatively small $E_{n\to\pi^*}$ values, while the remaining metal ions show values ranging from 0.25 to 1.44 kcal mol^{-1}. Notably, six metal ions—Sc^{3+}, Ti^{4+}, Fe^{2+}, Co^{2+}, Ni^{2+}, and Zn^{2+}—exhibit $E_{n\to\pi^*}$ values for $[M(L^{I2})_3]^{n+}$ that are comparable to or stronger than that of Co^{3+}. Among these, Co^{2+} and Ni^{2+} show the highest values, both exceeding 1.4 kcal mol^{-1}. However, for Sc^{3+}, Ti^{2+}, and Zn^{2+}, the distance between the pyrimidyl N and the C=N group on the adjacent L^{I2} exceeds the sum of the van der Waals radii of C and N, suggesting weaker interactions. In

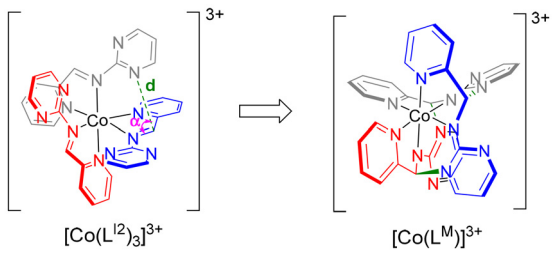

Fig. 5 Comparison of the energy difference between $[Co(L^M)]^{3+}$ (right) and $[Co(L^{I2})_3]^{3+}$ (left), calculation of $E_{n\to\pi^*}$ and the Bürgi–Dunitz parameters (α (°), d (Å)) for $[Co(L^{I2})_3]^{3+}$.

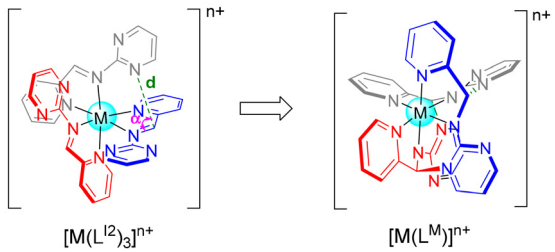

Fig. 6 Comparison of the energy difference between $[M(L^M)]^{n+}$ (right) and $[M(L^{I2})_3]^{n+}$ (left), calculation of $E_{n\to\pi^*}$ and the Bürgi–Dunitz parameters (α (°), d (Å)) for $[M(L^{I2})_3]^{n+}$.

Table 1 The DFT calculation of ΔE, $E_{n\rightarrow\pi^*}$ NBO and Bürgi-Dunitz trajectory parameters

	ΔE^a	$E_{n\rightarrow\pi^*}{}^b$	α^c	d^d
Sc^{3+}	5.73	0.76	110.7	3.48
Ti^{2+}	15.87	0.08	100.2	3.54
Ti^{4+}	−22.99	0.89	100.3	3.24
V^{2+}	8.37	0.24	89.3	3.25
Cr^{2+}	7.95	0.31	76.9	3.00
Mn^{2+}	0.85	0.14	77.6	3.01
Fe^{2+}	−3.64	1.01	74.3	2.94
Fe^{3+}	−24.05	0.34	70.0	2.80
Co^{2+}	0.65	1.43	68.5	3.00
Co^{3+}	−24.49	0.58	86.4	2.77
Ni^{2+}	2.93	1.44	79.6	3.11
Cu^{2+}	7.24	0.25	77.5	3.26
Zn^{2+}	10.79	0.89	97.8	3.48
Al^{3+}	−16.58	0.32	83.4	3.08

[a] Comparison of the energy (kcal mol^{-1}) difference between $[ML^M]^{n+}$ and $[M(L^{I2})_3]^{n+}$. [b] Calculation of $E_{n\rightarrow\pi^*}$ (kcal mol^{-1}). [c] The Bürgi-Dunitz angles α (°) in $[M(L^{I2})_3]^{n+}$. [d] The $N_{pym}\cdots C_{imine}$ d (Å) in $[M(L^{I2})_3]^{n+}$.

terms of stability, only $[Ti(L^M)]^{4+}$, $[Fe(L^M)]^{3+}$, and $[Al(L^M)]^{3+}$exhibit comparable stability to $[Co(L^M)]^{3+}$ when using $[M(L^{I2})_3]^{n+}$ as the reference. Although $[V(L^M)]^{2+}$ and $[Fe(L^M)]^{2+}$ are also more stable than their corresponding $[M(L^{I2})_3]^{n+}$, the differences are within 10 kcal mol^{-1}. For the remaining metal ions, $[M(L^{I2})_3]^{n+}$ is the more stable species. Interestingly, $[Co(L^M)]^{2+}$ is slightly less stable than $[Co(L^{I2})_3]^{2+}$ by 0.65 kcal mol^{-1}. Given that the starting material for $[Co(L^M)]^{3+}$ is Co(II), the formation of the highly stable $[Co(L^M)]^{3+}$ in CH_3CN likely drives the reaction forward under aerobic conditions.

Iron(III) as the template

Based on DFT calculations, Fe(III) was chosen as a template to explore whether a macrocyclic complex analogue to $[Co(L^M)]^{3+}$ could be formed. However, unexpectedly, when the reaction was conducted under conditions similar to those used for synthesizing $[Co(L^M)]^{3+}$, but with $Fe(ClO_4)_3{\cdot}6H_2O$ as the metal source, a pyridinium salt, *cis*-$[(L^{I2})_2](ClO_4)$, was isolated along with unidentified Fe(III)-containing products (Scheme 10). The crystal structure of *cis*-$[(L^{I2})_2](ClO_4)$, shown in Fig. 7, suggests that the presence of the $Fe(ClO_4)_3{\cdot}6H_2O$ may promote the dimerization of L^{I2} in a *cis* configuration. Based on these observations, it is possible that the coordination environment and ligand orientation prior to dissociation may influence whether the system evolves toward macrocyclization or dimerization; however, this aspect remains unclear and is currently being investigated. The detailed mechanism and the stereoselectivity of this reaction are currently under investigation.

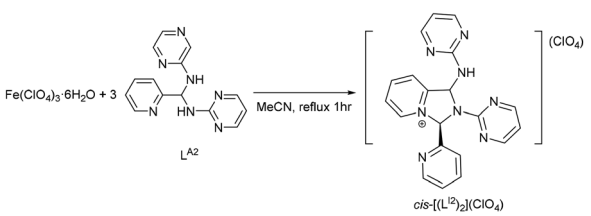

Scheme 10 Synthesis of *cis*-$[(L^{I2})_2](ClO_4)$.

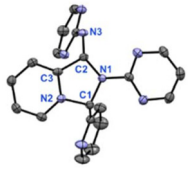

Fig. 7 ORTEP drawing of *cis*-$[(L^{I2})_2](ClO_4)$. The counteranion (ClO_4^-) and hydrogen atoms are omitted for clarity. Thermal ellipsoids are displayed at 50% probability level. Selected bond lengths (Å) and bond angles (°) for *cis*-$[(L^{I2})_2](ClO_4)$: N2–C1: 1.490(2); N1–C1: 1.451(2); N1–C2: 1.479(2); N3–C2: 1.429(2); N3–C2–C3: 114.73(15); C2–C3–N2: 110.67 (15); C2–N1–C1: 113.21(14); N1–C1–N2: 101.50(14).

Conclusions

In this study, we demonstrated that solvent and metal ion choice direct picolyl heterocyclic aminals into divergent coordination outcomes, including fluxional hemiaminalates, hemiaminal ethers, a Co(III)-templated polyazamacrocyclic complex, and an Fe(III)-induced pyridinium salt. A central finding is that coordination can stabilize inherently dynamic ligand forms, such as hemiaminals and hemiaminal ethers, enabling their isolation and structural characterization. This principle highlights how dynamic covalent scaffolds, often considered too labile for study, can become accessible through metal coordination.

By integrating reversibility with coordination, these systems reveal an expanded dimension of structural diversity in small-molecule chemistry. Unlike classical ligands, which deliver predictable geometries, dynamic aminals adapt their form in response to metal ions and solvents, giving rise to orthogonal reactivity pathways and unanticipated structures. This ability of coordination to both stabilize and redirect dynamic species enriches the conceptual framework of coordination chemistry diversity.

Beyond fundamental interest, such adaptive scaffolds provide a versatile platform for designing responsive functional complexes. Future work will extend this strategy to other metal ions and evaluate their potential in catalysis, molecular recognition, and biomedical applications.

Author contributions

J. W. J.: writing – original draft, writing – review & editing, validation, formal analysis, investigation, data curation, visualization. J. M. C.: writing – original draft, formal analysis, investigation, data curation, visualization. Y. R. H.: writing – review & editing, software, formal analysis, data curation, visualization. Y. F. L.: writing – original draft, writing – review & editing, conceptualization, methodology, visualization, resources, supervision, project administration, funding acquisition.

Conflicts of interest

There are no conflicts to declare.

Data availability

All remaining data are provided in the article and supplementary information (SI). Supplementary information is available. The SI contains synthetic procedures, additional experimental details, full characterization data (NMR, IR, UV–Vis, HR-ESI-MS), variable-temperature NMR studies, crystallographic information files (CIFs), supplementary figures and tables, and computational details. See DOI: https://doi.org/10.1039/d5dt02405f.

CCDC 2423656–2423658, 2493551–2493557, 2493743 contain the supplementary crystallographic data for this paper.[77a–k]

Acknowledgements

We sincerely appreciate the financial support from the National Science and Technology Council (NSTC), Taiwan, through research grants NSTC 111-2621-M-A49-004-MY3, NSTC 112-2113-M-259-007, NSTC 113-2113-M-259-005 and NSTC 114-2113-M-259-002. We also extend our gratitude to the National Center for High-performance Computing (NCHC), Taiwan, for providing computational and storage resources. Special thanks go to Dr Chien-Hung Liao and Mr Wei-Rong Yen for their assistance with single-crystal X-ray diffraction measurements. We thank the Advanced Instrumentation Center of the Department of Medical Research, Hualien Tzu Chi Hospital, Buddhist Tzu Chi Medical Foundation, and the Bioinnovation Center, Buddhist Tzu Chi Medical Foundation, Hualien, Taiwan, for access to mass spectrometry facilities, as well as Dr. Hsueh-Hui Yang for support with high-resolution ESI-MS analyses. We are deeply grateful to Department of Chemistry at National Taiwan University and Institute of Chemistry, Academia Sinica, for generously providing laboratory space, instrumentation, and research facilities. Their support made it possible for us to continue our research following the 2024 post-earthquake fire, which tragically destroyed the entire Chemistry Department building at NDHU.

References

1 T. Kano, T. Yurino, D. Asakawa and K. Maruoka, *Angew. Chem., Int. Ed.*, 2013, **52**, 5532–5534.
2 Y.-Y. Huang, C. Cai, X. Yang, Z.-C. Lv and U. Schneider, *ACS Catal.*, 2016, **6**, 5747–5763.
3 T. Yurino, Y. Aota, D. Asakawa, T. Kano and K. Maruoka, *Tetrahedron*, 2016, **72**, 3687–3700.
4 J. F. Bai, H. Sasagawa, T. Yurino, T. Kano and K. Maruoka, *Chem. Commun.*, 2017, **53**, 8203–8206.
5 M. E. Belowich and J. F. Stoddart, *Chem. Soc. Rev.*, 2012, **41**, 2003–2024.
6 Y. Zhou, L. Li, H. Ye, L. Zhang and L. You, *J. Am. Chem. Soc.*, 2016, **138**, 381–389.
7 J.-M. Ciou, H.-F. Zhu, C.-W. Chang, J.-Y. Chen and Y.-F. Lin, *RSC Adv.*, 2020, **10**, 40421–40427.
8 Z. Feng, S. Jia, H. Chen and L. You, *Tetrahedron*, 2020, **76**, 131128.
9 C. Palomo, J. M. Aizpurua, I. Ganboa and M. Oiarbide, *Eur. J. Org. Chem.*, 1999, 3223–3235.
10 I. Banik, F. F. Becker and B. K. Banik, *J. Med. Chem.*, 2003, **46**, 12–15.
11 S. F. Martin, *Pure Appl. Chem.*, 2009, **81**, 195–204.
12 L. A. Joyce, E. C. Sherer and C. J. Welch, *Chem. Sci.*, 2014, **5**, 2855–2861.
13 A. L. Berhanu, Gaurav, I. Mohiuddin, A. K. Malik, J. S. Aulakh, V. Kumar and K.-H. Kim, *TrAC Trends Anal. Chem.*, 2019, **116**, 74–91.
14 S. L. Pilicer, M. Mancinelli, A. Mazzanti and C. Wolf, *Org. Biomol. Chem.*, 2019, **17**, 6699–6705.
15 R. Lopez and C. Palomo, *Chemistry*, 2021, **27**, 20–29.
16 U. Krishnan and S. K. Iyer, *Photochem. Photobiol.*, 2022, **98**, 843–855.
17 X. Qu and Z. Yang, *Chem. – Asian J.*, 2016, **11**, 2633–2641.
18 S. J. Rowan, S. J. Cantrill, G. R. Cousins, J. K. Sanders and J. F. Stoddart, *Angew. Chem., Int. Ed.*, 2002, **41**, 898–952.
19 S. Otto, *J. Mater. Chem.*, 2005, **15**, 3357–3361.
20 L. You, *Chem. Commun.*, 2023, **59**, 12943–12958.
21 N. Boehnke, C. Cam, E. Bat, T. Segura and H. D. Maynard, *Biomacromolecules*, 2015, **16**, 2101–2108.
22 W. Dai, F. Shao, J. Szczerbiński, R. McCaffrey, R. Zenobi, Y. Jin, A. D. Schlüter and W. Zhang, *Angew. Chem., Int. Ed.*, 2016, **55**, 213–217.
23 H. Zhang, Z. Su and X. Wang, *ACS Sustainable Chem. Eng.*, 2022, **10**, 8650–8657.
24 P. Shen, B. Pollard, M. Ueland, D. Lawes and L. A. Connal, *Macromol. Rapid Commun.*, 2025, **46**, e2400683.
25 C. A. Zentner, F. Anson, S. Thayumanavan and T. M. Swager, *J. Am. Chem. Soc.*, 2019, **141**, 18048–18055.
26 F. L. C. Morgan, I. A. O. Beeren, J. Bauer, L. Moroni and M. B. Baker, *J. Am. Chem. Soc.*, 2024, **146**, 27499–27516.
27 A. Chao, I. Negulescu and D. Zhang, *Macromolecules*, 2016, **49**, 6277–6284.
28 F. García, J. Pelss, H. Zuilhof and M. M. J. Smulders, *Chem. Commun.*, 2016, **52**, 9059–9062.
29 F. Haase, E. Troschke, G. Savasci, T. Banerjee, V. Duppel, S. Dörfler, M. M. J. Grundei, A. M. Burow, C. Ochsenfeld, S. Kaskel and B. V. Lotsch, *Nat. Commun.*, 2018, **9**, 2600.
30 H. Yang, S. Ghiassinejad, E. van Ruymbeke and C.-A. Fustin, *Macromolecules*, 2020, **53**, 6956–6967.
31 F. Song, Z. Li, P. Jia, M. Zhang, C. Bo, G. Feng, L. Hu and Y. Zhou, *J. Mater. Chem. A*, 2019, **7**, 13400–13410.
32 J. Sun, H. He, K. Zhao, W. Cheng, Y. Li, P. Zhang, S. Wan, Y. Liu, M. Wang, M. Li, Z. Wei, B. Li, Y. Zhang, C. Li, Y. Sun, J. Shen, J. Li, F. Wang, C. Ma, Y. Tian, J. Su, D. Chen, C. Fan, H. Zhang and K. Liu, *Nat. Commun.*, 2023, **14**, 5348.

33 R. J. Kearsey, A. Tarzia, M. A. Little, M. C. Brand, R. Clowes, K. E. Jelfs, A. I. Cooper and R. L. Greenaway, *Chem. Commun.*, 2023, **59**, 3731–3734.
34 M. He and J.-M. Lehn, *Chem. – Eur. J.*, 2021, **27**, 7516–7524.
35 A. van Dam, R. van Schendel, S. Gangarapu, H. Zuilhof and M. M. J. Smulders, *Chem. – Eur. J.*, 2023, **29**, e202301795.
36 S. Ghosh, R. J. Butcher and R. Angamuthu, *Inorg. Chim. Acta*, 2024, **570**, 122167.
37 H. H. Jo, R. Edupuganti, L. You, K. N. Dalby and E. V. Anslyn, *Chem. Sci.*, 2015, **6**, 158–164.
38 Y. Zhou, Y. Yuan, L. You and E. V. Anslyn, *Chem. – Eur. J.*, 2015, **21**, 8207–8213.
39 C. Kachi-Terajima, T. Shimoyama, T. Ishigami, M. Ikeda and Y. Habata, *Dalton Trans.*, 2018, **47**, 2638–2645.
40 S. Raje, N. Mondivagu, M. Chahal, R. J. Butcher and R. Angamuthu, *Chem. – Asian J.*, 2018, **13**, 1458–1466.
41 S. Purkait, P. Chakraborty, A. Frontera, A. Bauzá, E. Zangrando and D. Das, *New J. Chem.*, 2018, **42**, 12998–13009.
42 J. P. Saucedo-Vázquez, V. M. Ugalde-Saldívar, A. R. Toscano, P. M. H. Kroneck and M. E. Sosa-Torres, *Inorg. Chem.*, 2009, **48**, 1214–1222.
43 S. Raje, A. Koner, S. Ghosh, R. J. Butcher, L. Mathivathanan, M. Sundararajan and R. Angamuthu, *Chem. – Asian J.*, 2023, **18**, e202300706.
44 L. You, S. R. Long, V. M. Lynch and E. V. Anslyn, *Chemistry*, 2011, **17**, 11017–11023.
45 M. Chahal, K. Mani, C. S. Lodhi, R. J. Butcher, S. Raje and R. Angamuthu, *ChemistrySelect*, 2018, **3**, 9960–9964.
46 L. You, S. R. Long, V. M. Lynch and E. V. Anslyn, *Chemistry*, 2011, **17**, 11017–11023.
47 Y. Zhou, Y. Ren, L. Zhang, L. You, Y. Yuan and E. V. Anslyn, *Tetrahedron*, 2015, **71**, 3515–3521.
48 N. Arulsamy and D. J. Hodgson, *Inorg. Chem.*, 1994, **33**, 4531–4536.
49 H. Adams, M. S. Shongwe, I. Al-Bahri, E. Al-Busaidi and M. J. Morris, *Acta Crystallogr., Sect. C:Cryst. Struct. Commun.*, 2005, **61**, m497–m500.
50 S. Ding, C. Xia, Y. Ji, Z. Liu and Y. Ding, *Acta Crystallogr., Sect. C:Cryst. Struct. Commun.*, 2011, **67**, m622–m623.
51 S. K. Padhi, R. Sahu and V. Manivannan, *Inorg. Chim. Acta*, 2011, **367**, 57–63.
52 S. Albano, G. Olivo, L. Mandolini, C. Massera, F. Ugozzoli and S. Di Stefano, *J. Org. Chem.*, 2017, **82**, 3820–3825.
53 C. E. Check, T. O. Faust, J. M. Bailey, B. J. Wright, T. M. Gilbert and L. S. Sunderlin, *J. Phys. Chem. A*, 2001, **105**, 8111–8116.
54 S. Grimme, J. Antony, S. Ehrlich and H. Krieg, *J. Chem. Phys.*, 2010, **132**, 154104.
55 M. J. Frisch, G. W. Trucks, H. B. Schlegel, G. E. Scuseria, M. A. Robb, J. R. Cheeseman, G. Scalmani, V. Barone, G. A. Petersson, H. Nakatsuji, X. Li, M. Caricato, A. V. Marenich, J. Bloino, B. G. Janesko, R. Gomperts, B. Mennucci, H. P. Hratchian, J. V. Ortiz, A. F. Izmaylov, J. L. Sonnenberg, D. Williams-Young, F. Ding, F. Lipparini, F. Egidi, J. Goings, B. Peng, A. Petrone, T. Henderson, D. Ranasinghe, V. G. Zakrzewski, J. Gao, N. Rega, G. Zheng, W. Liang, M. Hada, M. Ehara, K. Toyota, R. Fukuda, J. Hasegawa, M. Ishida, T. Nakajima, Y. Honda, O. Kitao, H. Nakai, T. Vreven, K. Throssell, J. A. Montgomery Jr., J. E. Peralta, F. Ogliaro, M. J. Bearpark, J. J. Heyd, E. N. Brothers, K. N. Kudin, V. N. Staroverov, T. A. Keith, R. Kobayashi, J. Normand, K. Raghavachari, A. P. Rendell, J. C. Burant, S. S. Iyengar, J. Tomasi, M. Cossi, J. M. Millam, M. Klene, C. Adamo, R. Cammi, J. W. Ochterski, R. L. Martin, K. Morokuma, O. Farkas, J. B. Foresman and D. J. Fox, *Gaussian 16 Rev. C.01*, in Wallingford, CT, 2016.
56 N. G. Connelly, T. Damhus, R. M. Hartshorn and A. T. Hutton, *Nomenclature of Inorganic Chemistry: IUPAC Recommendations 2005*, IUPAC and the Royal Society of Chemistry, Cambridge, 2005.
57 M. Bröring, S. Prikhodovski, C. D. Brandt, E. Cónsul Tejero, S. Köhler and C. Pietzonka, *Inorg. Chem.*, 2007, **46**, 917–925.
58 G. Bottomley, I. Clark, I. Creaser, L. Engelhardt, R. Geue, K. Hagen, J. Harrowfield, G. Lawrance, P. Lay, A. Sargeson, A. See, B. Skelton, A. White and F. Wilner, *Aust. J. Chem.*, 1994, **47**, 143–179.
59 P. Osvath, A. M. Sargeson, A. McAuley, R. E. Mendelez, S. Subramanian, M. J. Zaworotko and L. Broge, *Inorg. Chem.*, 1999, **38**, 3634–3643.
60 H. Ferreira, M. M. Conradie and J. Conradie, *Electrochim. Acta*, 2018, **292**, 489–501.
61 J. N. McPherson, R. W. Hogue, F. S. Akogun, L. Bondi, E. T. Luis, J. R. Price, A. L. Garden, S. Brooker and S. B. Colbran, *Inorg. Chem.*, 2019, **58**, 2218–2228.
62 J. P. F. Rebolledo-Chávez, G. T. Toral, V. Ramírez-Delgado, Y. Reyes-Vidal, M. L. Jiménez-González, M. Cruz-Ramírez, A. Mendoza and L. Ortiz-Frade, *Catalysts*, 2021, **11**, 948.
63 J. Yang, M. Ansari, D. A. Pantazis, C. H. M. Zheng, R. McDonald, M. J. Ferguson and L. Rosenberg, *Inorg. Chem.*, 2024, **63**, 22409–22421.
64 L. Rocchetti, A. Amato and F. Beolchini, *J. Clean. Prod.*, 2016, **116**, 299–305.
65 J. P. Reddy, *Acta Crystallogr. E*, 2020, **76**, 1771–1774.
66 G.-B. Li, B.-Q. Song, S.-Q. Wang, L.-M. Pei, S.-G. Liu, J.-L. Song and Q.-Y. Yang, *ACS Omega*, 2019, **4**, 1995–2000.
67 N. Podjed, J. Črepinšek and B. Modec, *Molbank*, 2021, **2021**, M1216.
68 P. C. Bell and J. D. Wallis, *Chem. Commun.*, 1999, 257–258.
69 A. Lari, M. B. Pitak, S. J. Coles, G. J. Rees, S. P. Day, M. E. Smith, J. V. Hanna and J. D. Wallis, *Org. Biomol. Chem.*, 2012, **10**, 7763–7779.
70 J. O'Leary and J. D. Wallis, *Org. Biomol. Chem.*, 2009, **7**, 225–228.
71 R. W. Newberry and R. T. Raines, *Acc. Chem. Res.*, 2017, **50**, 1838–1846.
72 H. B. B:urgi, J. D. Dunitz, J. M. Lehn and G. Wipff, *Tetrahedron*, 1974, **30**, 1563–1572.
73 H. B. Burgi, J. D. Dunitz and E. Shefter, *J. Am. Chem. Soc.*, 1973, **95**, 5065–5067.

74 H. Zheng, H. Ye, X. Yu and L. You, *J. Am. Chem. Soc.*, 2019, **141**, 8825–8833.
75 H. R. Kilgore, C. R. Olsson, K. A. D'Angelo, M. Movassaghi and R. T. Raines, *J. Am. Chem. Soc.*, 2020, **142**, 15107–15115.
76 K. B. Muchowska, D. J. Pascoe, S. Borsley, I. V. Smolyar, I. K. Mati, C. Adam, G. S. Nichol, K. B. Ling and S. L. Cockroft, *Angew. Chem., Int. Ed.*, 2020, **59**, 14602–14608.
77 (*a*) CCDC 2423656: Experimental Crystal Structure Determination, 2025, DOI: 10.5517/ccdc.csd.cc2mc0gh; (*b*) CCDC 2423657: Experimental Crystal Structure Determination, 2025, DOI: 10.5517/ccdc.csd.cc2mc0hj; (*c*) CCDC 2423658: Experimental Crystal Structure Determination, 2025, DOI: 10.5517/ccdc.csd.cc2mc0jk; (*d*) CCDC 2493551: Experimental Crystal Structure Determination, 2025, DOI: 10.5517/ccdc.csd.cc2ppr49; (*e*) CCDC 2493552: Experimental Crystal Structure Determination, 2025, DOI: 10.5517/ccdc.csd.cc2ppr5b; (*f*) CCDC 2493553: Experimental Crystal Structure Determination, 2025, DOI: 10.5517/ccdc.csd.cc2ppr6c; (*g*) CCDC 2493554: Experimental Crystal Structure Determination, 2025, DOI: 10.5517/ccdc.csd.cc2ppr7d; (*h*) CCDC 2493555: Experimental Crystal Structure Determination, 2025, DOI: 10.5517/ccdc.csd.cc2ppr8f; (*i*) CCDC 2493556: Experimental Crystal Structure Determination, 2025, DOI: 10.5517/ccdc.csd.cc2ppr9g; (*j*) CCDC 2493557: Experimental Crystal Structure Determination, 2025, DOI: 10.5517/ccdc.csd.cc2pprbh; (*k*) CCDC 2493743: Experimental Crystal Structure Determination, 2025, DOI: 10.5517/ccdc.csd.cc2ppybp.